Montoya, A., Rodríguez-Sánchez, M., López-Puente, J. & Santana, D. (2020). Influence of longitudinal clips in thermal stresses and deflection in solar tubular receivers. *Solar Energy, vol. 198*, pp. 224–238.

DOI: 10.1016/j.solener.2020.01.030

Influence of longitudinal clips in thermal stresses and deflection in solar tubular receivers

Andrés Montoya[a,*], M.R. Rodríguez-Sánchez[b], Jorge López-Puente[a], Domingo Santana[b]

[a] *Continuum Mechanics and Structural Analysis Department, Universidad Carlos III de Madrid, Avda. de la Universidad, 30, 28911 Leganés, Madrid, Spain*
[b] *Department of Thermal and Fluid Engineering, Universidad Carlos III de Madrid, Avda. de la Universidad, 30, 28911 Leganés, Madrid, Spain*

Abstract

Mechanical boundary conditions in tubular receivers of solar power tower plants have a main role in the thermal stress distribution and tube deflection. Longitudinal supports, particularly, has an strong influence on stress and displacements, since they prevent the tube bending.

In this work, the influence of longitudinal supports, on tube deflection and stress has been studied in external-cylindrical receivers, using an analytical methodology, which it is able to take into account the tube geometry in the deflection calculation. Therefore, real tube geometry with elbows can be considered. Results for two aiming strategies, one equatorial and another that flattens the heat flux, have been compared for different clips distances, from 1 to 9 meters.

The analytical methodology developed in Matlab provides lower computational cost than the numerical model developed in Abaqus. Results show

*Corresponding author.
Email address: andmonto@ing.uc3m.es (Andrés Montoya)

that clip distribution has a significant impact on thermal stress. For clips distance of 2 meters or lower, the generalised plane strain solution provides the stress distribution along the tube accurately, with a tube deflection lower than 1 millimetrer. When clips distance increases, the longitudinal stress distribution differs from the plane strain case, and the deflection increases to non-desirable values. Deflection is greater at tube ends, and aiming strategies that flatten the heat flux increases the displacement in that regions.
Keywords: Solar external-cylindrical receiver, Thermal stress, Analytical model, Longitudinal supports, Deflection, Tube elbows

1. Introduction

Central receivers are a main component of solar power tower plants (Ho, 2017). In these plants, an heliostat field aims the sunlight over the central receiver. The receiver is composed by panels of tubes, with a heat-transfer fluid (HTF) flowing through them. The HTF is heated by the incident solar radiation over the panels and then used as a heat source for the power generation system.

In this work, a receiver with a cylindrical shape has been studied. The non-homogeneus solar flux over the receiver panels causes temperature gradients, leading to thermal stress and deformations in the tubes. The heat flux along the tubes is non-linear, with circumferential variations. Nevertheless, since an smooth axial temperature variation along the tube does not cause stress, as Irfan and Chapman (2009) presented, 2D analysis can be used to characterize thermal stresses in receiver tubes.

A cylinder under circumferential and radial temperature distributions is

a problem that has been studied widely in the literature. Several authors, as Timoshenko and Goodier (1951), Gatewood (1941), and especially Goodier (1937, 1957) developed useful formulation to calculate analytically thermal stresses in thin-walled cylindrical bodies. Marugán-Cruz et al. (2016) carried out a study of stress in thin-walled cylinder with Gatewood formulation, and Logie et al. (2018) synthesized a generalized plane-strain methodology to obtain the thermal stress in central receivers. In these works only the thermal stress caused by temperature gradients was studied, without considering mechanical boundary conditions along the receiver tubes. In this work, the influence of the mechanical boundary conditions in tube deflection will be studied.

To prevent excessive panel warpage and bowing (Radosevich and Skinrood, 1989), caused by the thermal gradients, tubes are attached to the receiver structure by longitudinal supports (McDowell and Miner, 2013), called clips (Fig. 1). The clips are attached to the tube individually, by a welding procedure, that limits the penetration to the tube wall to the minimum, just to assure the complete union.Jones (1979) claimed that a generalized plane-strain analysis should accurately reflect the state of stress and strain, when clips are close enough, except in those regions where thermal conditions are rapidly changing. However he did not analysed the influence of the clips distance in the tube deflection.

Although generalized plane strain analysis offers a good approximation to the thermal stress values, if the real mechanical boundary conditions are not considered, the location of the actual highest stress will not be provided correctly, caused by the deflection in the tube (Montoya et al., 2018). The

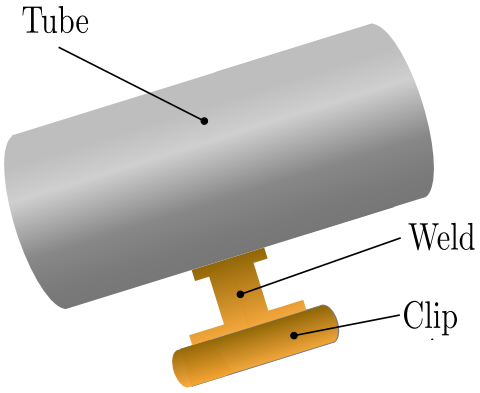

Fig. 1: Clip welded to the tube.

distance between tubes is small compared with its diameter, with typical values between 1 to 2.5 mm (Litwin, 2002). Therefore an excessive difference on the deflection of the tubes could make them collide, because the heat flux would not be axisymmetric.

Several thermomechanical 3D analyses were carried out in central receivers, although due to the complexity of the problem, some simplifications were made. Wang et al. (2012) used a numerical analysis to select the most adequate material in the receiver, but longitudinal supports were not considered. Du et al. (2016) focused their research on fatigue fracture, without considering mechanical restrictions. Uhlig et al. (2018) developed a 3D model of a complete receiver panel, although the high computational cost did not allow an in-depth stress analysis.

The tube bending phenomena has been deeply analyzed in parabolic through concentrators, where straight tubes are supported at multiple points. Wang et al. (2015) developed a CFD model to compute thermal stresses in a 2 m tube fixed on both ends. Li et al. (2017) did a similar study in 4

m and 8 m tube segments, also fixed on both ends, so the influence of supports along the length was not considered. The finite element model from Akbarimoosavi and Yaghoubi (2013) considered the longitudinal supports, although stress results were not provided in the study. Another model to calculate the solar flux distribution in the absorber tube, and its modification due to tube bending, was made by Khanna et al. (2013). The model was expanded in Khanna et al. (2014) to obtain deflection and stress in absorber tubes supported at multiple points. This analytical model was also compared with experimental results (Khanna et al., 2016) obtaining a good correlation between them.

The present work studies the tube bending phenomena in solar power tower cylindrical-external receivers using an analytical methodology. Unlike existing literature, it takes into account the existence of elbows in the edges of the receiver tubes for a better panel assembly and the mechanical supports (clips) location along the tube length. Results will be compared with other methodologies and a finite element model (FEM). The influence of supports distance on stresses and deflection will be also studied, for different aiming strategies, to find the clips distance threshold for considering a plane strain case.

This work is organized as follows: in the following section, the studied receiver and its boundary conditions are presented. Section 3 introduces the analytical methodology developed to perform the analysis. On section 4, the methodology is compared with existing methodologies, and it is verified with the FEM solution. Results for stress and tube deflection depending on clips distance and aiming strategy are also studied with the proposed methodology.

In the last section, conclusions from this work are summarized.

2. Studied problem

2.1. Central receiver characteristics

Thermal stresses and displacements of tubes in the receiver panels of a solar power tower plant with a cylindrical-external receiver, which uses molten salt as heat transfer fluid (HTF), has been studied. It is located in Tonopah (Nevada, EEUU), at a 38.24° North latitude, and it has a nominal power of 150 MWe. The most significant parameters of the solar field and the receiver are summarized in Table 1.

Table 1: Parameters for the studied solar plant..

Parameter	Value
Number of heliostats	10300
Heliostat dimensions	11.28×10.36 [m]
Latitude	38.24°
Tower height	195 [m]
Receiver length	30.5 [m]
Receiver diameter	17.6 [m]
Number of panels	18
Tubes per panel	127
Tubes separation	1.8 [mm]
Tube length	20.3 [m]
Outer tube diameter	22.4 [mm]
Tube thickness	1.2 [mm]
HTF inlet temperature	563 [K]
HTF outlet temperature	838 [K]
Mass flow rate (per tube)	3.98 [kg/s]
Ambient temperature	298 [K]

The solar field layout, composed of 10300 heliostats surrounding the tower, have been obtained from (Rodriguez-Sanchez et al., 2014). While

reflectivity, cleanliness and tracking errors of the mirros have been obtained from Sánchez-González et al. (2017). Tower height is 195 m, with a receiver of 30.5 m height at the top of it. The HTF thermal properties (60% $NaNO_3$ - 40% KNO_3), have been obtained from Zavoico (2001).

The solar external receiver is formed by 18 vertical panels, arranged in a cylindrical shape. Each panel is formed by an inlet header, a set of 127 tubes, and an outlet header. Each tube is individually welded to both headers by its edges. The panels are supported at the top header, which is fixed to the receiver frame. The bottom header can displace in the downward direction, allowing the free thermal expansion of the tubes. The tubes have a straight length of 18 m, irradiated by the solar flux reflected from the heliostats. To decrease the gap between tubes and to increase the heat transfer surface, tubes have a non-irradiated zone with different elbows configuration, connecting the straight length with the top and bottom headers. An example of the tube geometry is shown in 2, with the HTF inlet in the top header. To both guiding the tube and preventing the contact between tubes, mechanical supports, called clips, are welded to the rear side of the tube straight region, connecting the tubes with the receiver frame. The clips have been assumed as mobile supports in the longitudinal direction, only restricting the displacement perpendicular to the tube length.

The receiver tubes have an external diameter of 22.4 mm, and a wall thickness of 1.2 mm. The distance between tubes is 1.8 mm (8% of its diameter.) The receiver tubes are made of Inconel alloy 625 (American Society of Mechanical Engineers, 2010), coated with black Pyromark 2500 on its outer surface, to increase the absorptivity. Besides, to minimize heat losses

the receiver frame consists on a refractory wall that reflects and reradiates the solar flux to the tubes.

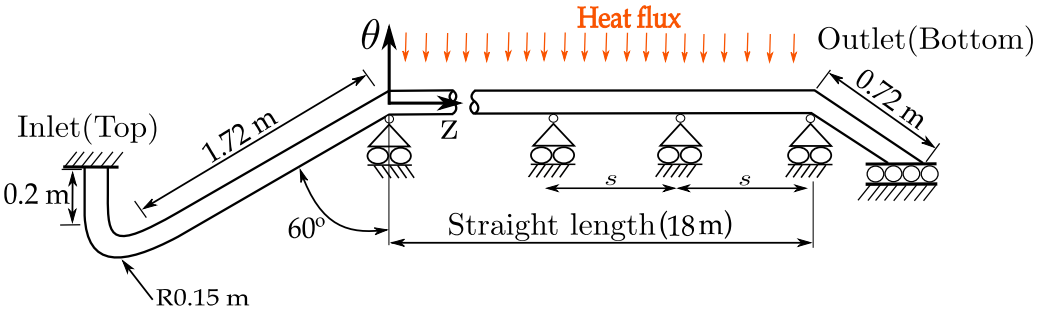

Fig. 2: Tube geometry schematic and boundary conditions. Clips are separated by a uniform distance s.

The HTF flows in parallel by all the 127 tubes of each panel, and in series by the different panels of the receiver. Therefore, the fluid enters at the receiver by the bottom edge of the first panel tubes, leaving the panel from the top side, and entering the following panel from the top header, and so on. The receiver is formed by two flow paths, comprising each half of the panels. As the plant is in the North hemisphere, the HTF enters the receiver by the two northern panels and exits by the two southern panels. To equalize the solar flux distribution in both sides of the receiver, there is a crossover between the two flow paths at the exit of the fifth panels, as Fig. 3 depicts. Note that the panel numbering depends on where the flow path starts, west or east.

2.2. Thermal conditions

Solar power towers are generally designed for the solar noon of the Spring Equinox, being the moment selected to carry out the receiver calculations.

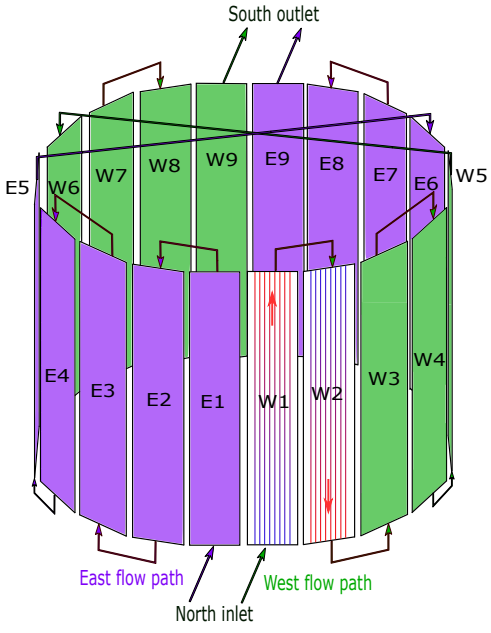

Fig. 3: Schematic of a receiver panels and flow path directions. Note that each color refers to a flow path: green for West (W) and purple for East (E).

In that moment, the receiver operates at nominal conditions and the thermal stresses have the highest daily value (Montoya et al., 2019). Montoya et al. (2019) also pointed out that the maximum stress corresponds to the northerm panels of the receiver, due to the low temperature of the heat transfer fluid and the high solar radiation. Therefore, the first panel of the receiver will be the one analyzed. The analytical model developed in this work needs the temperature profiles of the tube walls as input parameters. To obtain them, a thermo-optical model of the solar field and the receiver has been used.

The optical model FluxSPT[1] (Sánchez-González et al., 2018), developed in Matlab, has been used to calculate the solar flux distribution. It is based on

[1] `ise.uc3m.es/research/solar-energy/fluxspt`

the convolution-projection method developed and experimentally validated in (Sánchez-González and Santana, 2015). FluxSPT generates symmetric flux maps about the receiver equator and allows to modify the aiming strategy of the heliostats in a simple way, which connects the solar flux incident on the receiver and the spillage losses. The main characteristic of the model is that it is able to find an aiming strategy that the solar flux distribution in the axial direction. In this study, two aiming strategies, one equatorial and another that tries to flatten the heat flux along the tubes (flat aiming strategy), have been considered. The solar flux distribution in the straight length of the tubes, caused by each strategy is shown in Fig. 4.

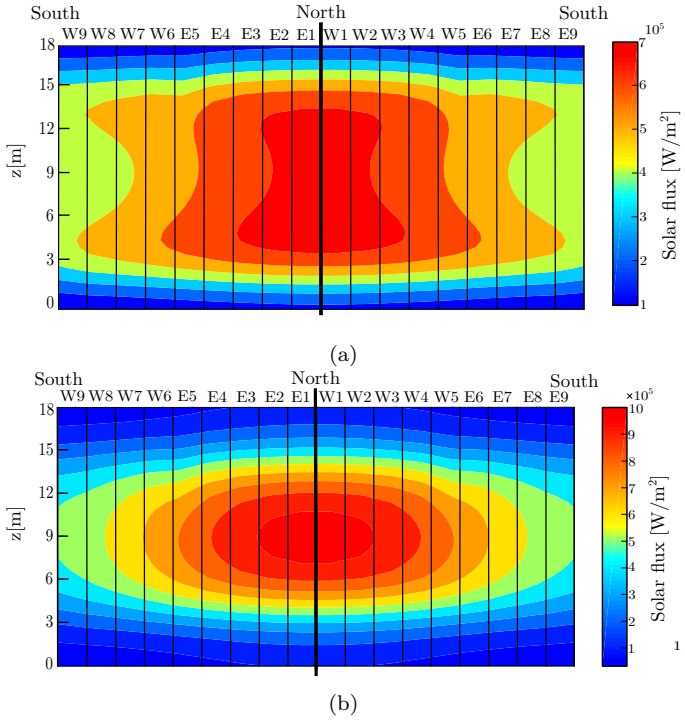

Fig. 4: Solar flux distribution on the receiver surface for a (a)flat aiming strategy (b) equatorial aiming strategy.

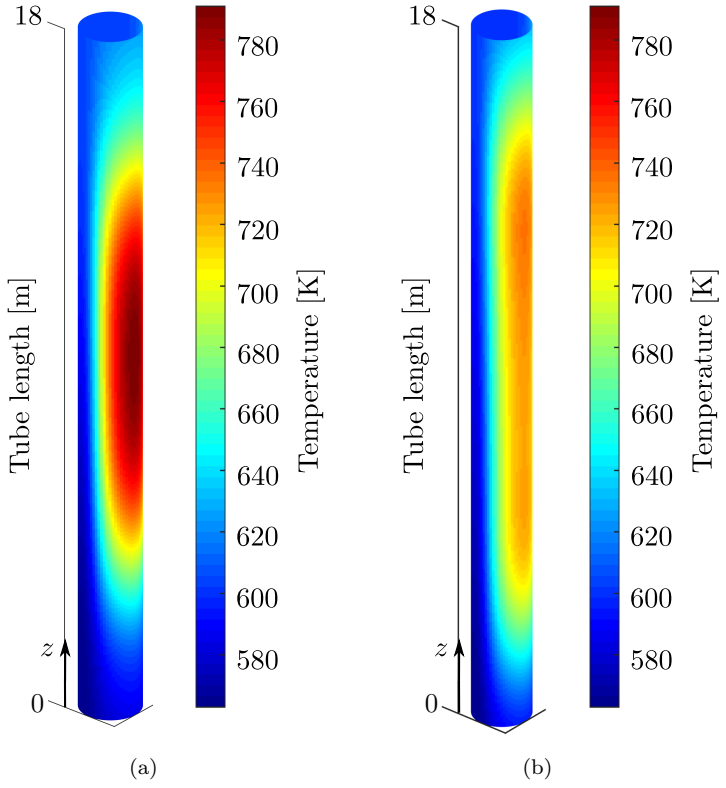

Fig. 5: Temperature profiles on the outer tube wall along the straight tube length for a a) equatorial aiming strategy, and a b) flat aiming strategy. The diameter is magnified for clarity

The thermal model developed by Rodríguez-Sánchez et al. (2014) allows the heat exchange and temperature distributions to be characterized in the receiver tubes. It is a steady-state thermal model based on energy balances and correlations, coded in Matlab. It solves the conjugate problem between the radiative and convective heat transfer on the tubes and the heat conduction in the tube walls. To do that, the tubes are discretized in axial and circumferential directions. This model needs as input parameters the solar flux distribution on the receiver surface, obtained with FlufSPT, but as a

simplification, the model assumes that all the tubes of a panel have the same heat flux and temperature distribution.

Fig. 5 depicts the outer wall temperature distribution for the selected aiming sstrategies, over the straight tube length in the first receiver panel (W1 or E1 from Figs. 3 and 4). Fig. 5a shows the wall temperature when heliostats are aimed to the receiver equator, therefore, the temperature is greater on the central receiver section facing the heliostats ($\theta = 0°$). Fig. 5a shows a less aggresive aiming strategy, where the heat flux along the receiver length has been flattened. The non-irradiated ends of the tube, not depicted in Fig. 5, have the same temperature than the HTF in the inlet and oulet of the straight zone of the tube (563 K entering the first panel, and 604 K leaving it.)

3. Analytical methodology

In order to obtain the longitudinal stress and deflection on receiver tubes, without considering a plane-strain problem and taking into account the actual tube geometry and boundary conditions, the following two-step analytical methodology is proposed. First, the displacements in the tube are calculated, to then obtain the thermal stress.

3.1. Tube deflection

The deflection of a straight tube supported at multiple points can be obtained using the same methodology proposed by Khanna et al. (2014). In the later procedure, the stiffness of the elbows located at the tube ends of central receivers is not taken into account in such methodology. To solve the displacement of the actual tube geometry, the direct stiffness method, also

known as the matrix stiffness method, applied to bidimensional structures made by beams, is used.

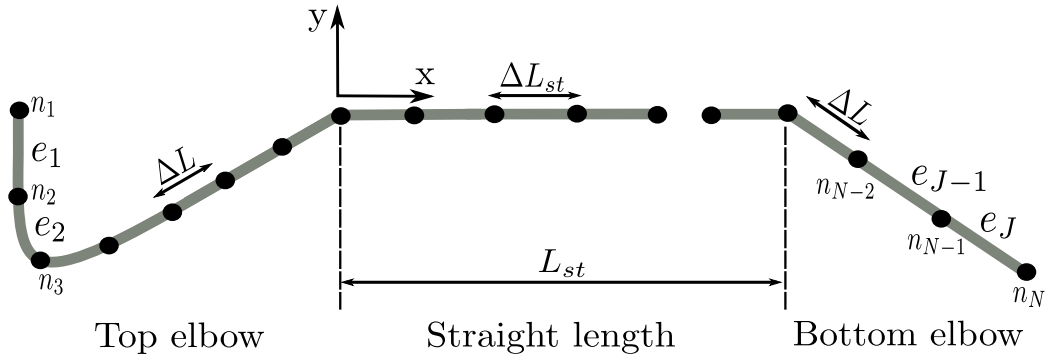

Fig. 6: Problem discretization in beam elements.

Direct stiffness method (Kassimali, 2011) is a matrix method that calculates the forces and displacements in a structure using the stiffness relations of the members that integrate the structure. The system is discretized as Fig. 6 shows: a set of beams elements $e = 1, 2...J$ of ΔL length at the elbows, and ΔL_{st} along the straight tube region. Elements are connected at the nodes $n = 1, 2...N$, being the number of nodes $N = J + 1$. Nodes are referenced to a cartesian coordinate system, with the same reference system origin as the cylindrical coordinate system depicted in Fig. 2.

Material properties of the elements and their interconnections are put together in a matrix equation which relates the displacement in the nodes with the forces through the stiffness matrix:

$$\vec{\mathbf{F}} = \mathbf{K}\vec{\mathbf{U}} \tag{1}$$

where $\vec{\mathbf{F}}$ is the nodal force vector, $\mathbf{K}$ corresponds to the global stiffness matrix, and $\vec{\mathbf{U}}$ represents the nodal displacement vector. Thus, Eq. 1 is a linear system of equations represented as a matrix equation, being the displacements in each node the unknown variables. To solve the problem, it is necessary first to calculate $\vec{\mathbf{F}}$ and $\mathbf{K}$.

3.1.1. Calculating the nodal forces

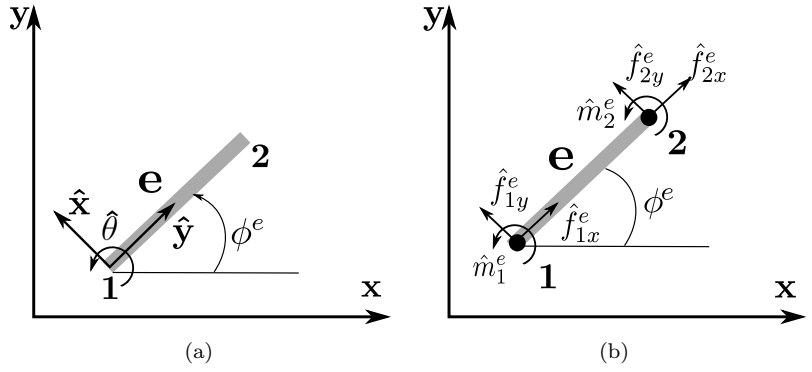

Fig. 7: a) Forces and moments in local coordinates for a beam e b) Local ($\hat{x}$,$\hat{y}$) and global (x,y) coordinates system of a element beam e. ϕ is the rotation angle of the element about the global coordinate system.

To construct the force vector $\vec{\mathbf{F}}$, the forces on each element have to be calculated. Each node n has 3 degrees of freedom (Fig. 7a): two displacement degrees of freedom $\hat{u}$ ($\hat{x}$ or $\hat{y}$ direction) and a rotation degree of freedom $\hat{\theta}$. Similarly, forces $\hat{f}$ on the nodes have $\hat{x}$ and $\hat{y}$ components, as Fig. 7b depicts, and a bending moment $\hat{m}$ can also be applied as a load. Therefore, the displacement vector $\hat{\vec{\mathbf{u}}}$ of an element e, and the element forces vector $\hat{\vec{\mathbf{f}}}$

are:

$$\hat{\vec{\mathbf{u}}}^e = \left(\begin{array}{c} \hat{u}^e_{1x} \\ \hat{u}^e_{1y} \\ \hat{\theta}^e_1 \\ \hline \hat{u}^e_{2x} \\ \hat{u}^e_{2y} \\ \hat{\theta}^e_2 \end{array}\right) \qquad \hat{\vec{\mathbf{f}}}^e = \left(\begin{array}{c} \hat{f}^e_{1x} \\ \hat{f}^e_{1y} \\ \hat{m}^e_1 \\ \hline \hat{f}^e_{2x} \\ \hat{f}^e_{2y} \\ \hat{m}^e_2 \end{array}\right) \tag{2}$$

Since in the direct stiffness method, loads only can be placed at the nodes, for each element, $\hat{\vec{\mathbf{f}}}^e$ is the sum of the external forces on the nodes $\hat{\vec{\mathbf{p}}}$ and the distributed forces along the beams transformed in nodal forces $\hat{\vec{\mathbf{r}}}$:

$$\hat{\vec{\mathbf{f}}}^e = \hat{\vec{\mathbf{p}}}^e + \hat{\vec{\mathbf{r}}}^e \tag{3}$$

For the studied problem, there are not nodal external loads $\hat{\vec{\mathbf{p}}}$, so only forces and bending moments due to temperature distribution are taken into account. Since thermal loads are located along the element beams, they have to be transformed in nodal forces and moments $\hat{\vec{\mathbf{r}}}$. In order to do that, the principle of superposition is used. The real displacements and stresses in the elements, as well as reaction forces and moments in the restricted nodes will be the sum of all the subproblems.

Fig. 8 depicts a beam element with a temperature increment ΔT, being the solution the sum of rigidly fixing both ends of the beam (encastred problem) and applying the temperature increment, to obtain the reactions at the nodes. The mentioned reactions from the encastred problem are applied at the nodes from the matrix problem with the opposite sign. In the case

studied, every element has its own temperature distribution. Therefore, the number of encastred problems will be the same as the number of elements in which the geometry has been discretized. To create the matrix problem, the sum of all the nodal forces from the encastred problems has to be added.

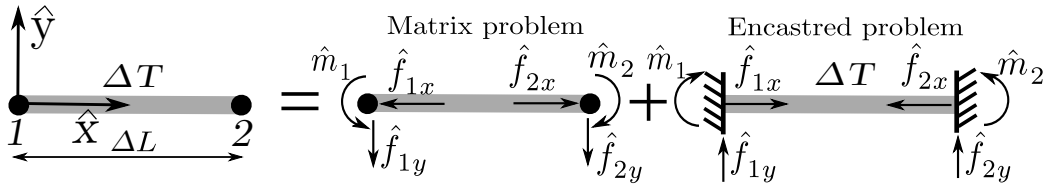

Fig. 8: Case of a beam with temperature increment, and its decomposition in two problems.

Thus, the value of $\hat{\vec{\mathbf{r}}}$ for each element is:

$$\hat{\vec{\mathbf{r}}}^e = \hat{\vec{\mathbf{f}}}^e_{matrix} = -\hat{\vec{\mathbf{f}}}^e_{enc} \tag{4}$$

For receiver tubes, two types of thermal loads, depending on the tube region, can be considered. In the top and bottom elbow regions, the temperature has been assumed as constant throughout the element cross-section and is equal to the HTF temperature, thus $\Delta T_{elbow} = T_{HTF} - T_{amb}$. Since no circumferential variation exists, the temperature increment produces only a thermal expansion of the beam. It is prevented by the rigidly fixed ends in the encastred problem, therefore, only reactions in the $\hat{x}$ direction exists, whose value is:

$$|\hat{f_{1x}}|_{elbow} = |\hat{f_{2x}}|_{elbow} = \alpha E A \Delta T_{elbow} \tag{5}$$

Where A is the cross section area of a cylindrical tube, α is the linear thermal expansion coefficient for the material and E the material Young's

modulus. The reactions of the encastred problem are compression forces, introduced as tension forces in the matrix problem, as Fig. 8 shows. Reactions forces in $\hat{y}$ direction and moments are null in the tube elbows regions.

On the other hand, the straight tube region is under the solar radiation reflected by the heliostats. As a result, the tube temperature varies longitudinally, radially and circumferentially, causing the tube bending. The inner, $T_{in}(r = a, \theta, z)$ and outer, $T_{out}(r = b, \theta, z)$ temperature profiles of the tube wall have been obtained with the receiver thermal model explained previously (Rodríguez-Sánchez et al., 2014). From those temperatures it is possible to obtain the temperature distribution in the straight tube length for any radial position, $T_{st}(r, \theta, z)$, assuming unidimensional diffusion of the heat:

$$T_{st}(r, \theta, z) = \frac{T_{in}(r = a, \theta), z - T_{out}(r = b, \theta, z)}{\ln \frac{a}{b}} \ln \frac{r}{b} + T_{out}(r = b, \theta, z) \quad (6)$$

When there is a temperature variation in the tube cross-section exists, a "thermal force" F_t appears (Barron and Barron, 2011), representing the fact that different regions of the cross-section tries to expand at a different rate, but it has to remain continuous. The reactions forces $\hat{f}_x$ at the ends of the beam has the same value as F_T, and can be expressed as:

$$|\hat{f_{1x}}|_{st} = |\hat{f_{2x}}|_{st} = F_T = \int_{-\pi}^{\pi} \int_{a}^{b} \alpha E \Delta T_{st} r \, dr d\theta \quad (7)$$

With $\Delta T_{st} = T_{st}(r, \theta) - T_{amb}$. In addition, there is thermal bending moment due to the temperature variation across the tube section (Barron

and Barron, 2011). Its value in each element can be calculated as:

$$M_T = \int_{-\pi}^{\pi} \int_{a}^{b} \alpha E \Delta T_{st} r^2 \cos\theta \, dr d\theta \tag{8}$$

A beam encastred at both ends (encastred problem, Fig. 8) with a uniform thermal moment along its length is a problem that can be solved with the following equilibrium of forces and moments:

$$\sum F_{\hat{y}} = \hat{f_{1y}} + \hat{f_{2y}} = 0 \tag{9}$$

$$\sum M(\hat{x} = 0) = -\hat{m}_1 + \hat{m}_2 + \hat{f_{2y}} \Delta L_{st} = 0 \tag{10}$$

where M is the expression for the bending moment along the segment, it is the sum of the thermal moments caused by the temperature variation $T_{st}(r, \theta)$, and the mechanical moments due to the reactions forces and moments that appear to prevent the tube deflection. From node 1 to 2, in local coordinates can be expressed as:

$$M(\hat{x}) = \hat{f_{1y}} x + M_T - \hat{m}_1 \tag{11}$$

Relating the bending moment expression with the displacement and rotations (Gere and Goodno, 2012) as:

$$\frac{d^2 \hat{u}_y(\hat{x})}{d\hat{x}^2} = \frac{M(\hat{x})}{EI} \tag{12}$$

$$\hat{\theta}(\hat{x}) = \frac{du_y(\hat{x})}{d\hat{x}} \tag{13}$$

More equations can be obtained, since rotation θ and displacement u_y are prevented at the element ends:

$$\hat{u}_y(\hat{x}) = 0 \quad \text{and} \quad \hat{\theta}(\hat{x}) = 0 \quad \text{for} \quad \begin{cases} \hat{x} = 0 \\ \hat{x} = \Delta L_{st} \end{cases} \tag{14}$$

Therefore, a system of 6 equations and 6 unknowns (4 reactions, 2 integration constants) can be solved. The solution for the reactions forces in the $\hat{y}$ direction is:

$$|\hat{f_{1y}}|_{st} = |\hat{f_{2y}}|_{st} = 0 \tag{15}$$

and the value of the moment reactions are:

$$|\hat{m_1}|_{st} = |\hat{m_2}|_{st} = M_T \tag{16}$$

The element reactions for the encastred problem in each tube region are summarized in Table 2. The force vectors for each element $\hat{\vec{\mathbf{f}}}^e$ can be calculated using these values and Eqs. 3 and 4.

Table 2: Values for the element forces and moments in elbows and straight length regions

	$\lvert\hat{f_{1x}}\rvert$	$\lvert\hat{f_{2x}}\rvert$	$\lvert\hat{f_{1y}}\rvert$	$\lvert\hat{f_{2y}}\rvert$	$\lvert\hat{m_1}\rvert$	$\lvert\hat{m_2}\rvert$
Elbows	$\alpha EA\Delta T_{elbow}$	$\alpha EA\Delta T_{elbow}$	0	0	0	0
Straight length	F_T	F_T	0	0	M_T	M_T

3.1.2. Assembling the global stiffness matrix

To assemble the global stiffness matrix, it is necessary to know the local stiffness matrix of each element. The local stiffness matrix $\hat{\mathbf{K}}^e$ has four submatrixes:

$$\hat{\mathbf{K}}^e = \left[\begin{array}{c|c} \hat{\mathbf{K}}^e_{11} & \hat{\mathbf{K}}^e_{12} \\ \hline \hat{\mathbf{K}}^e_{21} & \hat{\mathbf{K}}^e_{22} \end{array}\right] = \left[\begin{array}{ccc|ccc} \frac{EA}{L} & 0 & 0 & -\frac{EA}{L} & 0 & 0 \\ 0 & \frac{12EI}{L^3} & \frac{6EI}{L^2} & 0 & -\frac{12EI}{L^3} & \frac{6EI}{L^2} \\ 0 & \frac{6EI}{L^2} & \frac{4EI}{L} & 0 & -\frac{6EI}{L^2} & \frac{2EI}{L} \\ \hline -\frac{EA}{L} & 0 & 0 & \frac{EA}{L} & 0 & 0 \\ 0 & -\frac{12EI}{L^3} & -\frac{6EI}{L^2} & 0 & \frac{12EI}{L^3} & -\frac{6EI}{L^2} \\ 0 & \frac{6EI}{L^2} & \frac{2EI}{L} & 0 & -\frac{6EI}{L^2} & \frac{4EI}{L} \end{array}\right] \tag{17}$$

where L is the considered element length. To assemble the global stiffness matrix, which connects all the elements, it is necessary to transform the stiffness matrix of each element, from its local coordinate system to the global one (Fig. 7a). The transition matrix for a beam element ($\mathbf{T}^e$) has the following structure:

$$\mathbf{T}^e = \left[\begin{array}{ccc|ccc} \cos\phi & -\sin\phi & 0 & 0 & 0 & 0 \\ \sin\phi & \cos\phi & 0 & 0 & 0 & 0 \\ 0 & 0 & 1 & 0 & 0 & 0 \\ \hline 0 & 0 & 0 & \cos\phi & -\sin\phi & 0 \\ 0 & 0 & 0 & \sin\phi & \cos\phi & 0 \\ 0 & 0 & 0 & 0 & 0 & 1 \end{array}\right] \tag{18}$$

Using the transition matrix $\mathbf{T}^e$, stiffness matrix can be expressed in global

coordinates as follows:

$$\mathbf{K}^e = \mathbf{T}^e \hat{\mathbf{K}}^e \mathbf{T}^{e\intercal} \tag{19}$$

When the matrixes of each element have been transformed to global coordinates, global stiffness matrix $\mathbf{K}$ can be assembled. Due to the problem geometry, each node is connected to another two nodes maximum, as Fig. 6 depicts. Therefore, if there are J beam elements in the structure, from the previously described submatrixes of $\mathbf{K}^e$, $\mathbf{K}$ can be expressed as:

$$\mathbf{K} = \left[\begin{array}{c|c|c|c|c|c} \mathbf{K}_{11}^1 & \mathbf{K}_{12}^1 & \mathbf{0}_{3\times3} & \dots & \dots & \mathbf{0}_{3\times3} \\ \hline \mathbf{K}_{21}^1 & \mathbf{K}_{22}^1 + \mathbf{K}_{11}^2 & \mathbf{K}_{12}^2 & \ddots & \dots & \mathbf{0}_{3\times3} \\ \hline \mathbf{0}_{3x3} & \mathbf{K}_{21}^2 & \mathbf{K}_{22}^2 + \mathbf{K}_{11}^3 & \ddots & \ddots & \mathbf{0}_{3\times3} \\ \hline \vdots & \ddots & \ddots & \ddots & \ddots & \mathbf{0}_{3\times3} \\ \hline \vdots & \ddots & \ddots & \ddots & \mathbf{K}_{22}^{J-1} + \mathbf{K}_{11}^J & \mathbf{K}_{12}^J \\ \hline \mathbf{0}_{3\times3} & \mathbf{0}_{3\times3} & \mathbf{0}_{3\times3} & \mathbf{0}_{3\times3} & \mathbf{K}_{21}^J & \mathbf{K}_{22}^J \end{array}\right] \tag{20}$$

where $\mathbf{K}$ is a squared matrix of $3 \times N$ dimension, since 3 is the number of degrees of freedom of each node, and N is the number of nodes.

3.1.3. Displacements and reactions in the receiver tube

Using the transition matrix $\mathbf{T}^e$, element forces vector in global coordinates can be related to the ones in local coordinates as follows:

$$\vec{\mathbf{f}}^e = \mathbf{T}^e \hat{\vec{\mathbf{f}}}^e \tag{21}$$

$\vec{\mathbf{F}}$ is the sum of the nodal forces for each element, already calculated:

$$\vec{\mathbf{F}} = \sum_{e=1}^{J} \vec{\mathbf{f}}^{e} \tag{22}$$

where $\vec{\mathbf{F}}$ is a column vectors of $3 \times N$ size, the same as $\vec{\mathbf{U}}$. Defined $\vec{\mathbf{F}}$ and $\mathbf{K}$, a linear system of equations that solves the problem has been set (Eq. 1). In nodes where mechanical boundary conditions are located, the value of the displacements in the restricted degrees of freedom is null. Then, Eq. 1 solves the displacements for the matrix problem of Fig. 8. The displacements due to the temperature variation in the receiver tube are the same than in the matrix problem since nodal displacement for the encastred problem are null. No external forces are present in the original problem, therefore, the reaction forces in each node, needed to obtain the thermal stress along the tube, can be calculated as:

$$\vec{\mathbf{R}} = \mathbf{K}\vec{\mathbf{U}} + \sum_{e=1}^{J} \vec{\mathbf{f}}_{enc}^{e} \tag{23}$$

3.2. Longitudinal stress with clips

Once the nodal reactions have been calculated with the direct stiffness method, longitudinal stress along the straight tube length, where the solar radiation is concentrated by the heliostats, can be calculated. The equation for calculating the longitudinal stress in a beam under thermal loads (Barron and Barron, 2011) is:

$$\sigma_z = \frac{F_T}{A} + \left(\frac{M}{I}\right) r\cos\theta - \alpha E \Delta T \tag{24}$$

where M is the bending moment along the beam with multiple supports (Fig. 9), whose expression is similar to Khanna et al. Khanna et al. (2014) bending moment equation:

$$M(z) = M_{T1} - M_{top} + R_{top}(d_{top} + z) + \sum_{e=2}^{J}(M_{Te} - M_{Te-1})[\{z - (e-1)\Delta L_{st}\}^{+}]^{0} + \sum_{j=1}^{w} R_j[\{z - (j-1)d_j\}^{+}] \tag{25}$$

It is composed by the bendings moments produced by the reactions at the top tube end R_{top} and M_{top}, the bending moments from the clips reactions R_j, and the thermal beding moments M_{Te} on each e beam element, calculated with Eq. 8. d_j is the jth clip distance to the reference system origin. Since the clips are uniformly spaced with a distance s, $d_j = s(j-1)$.

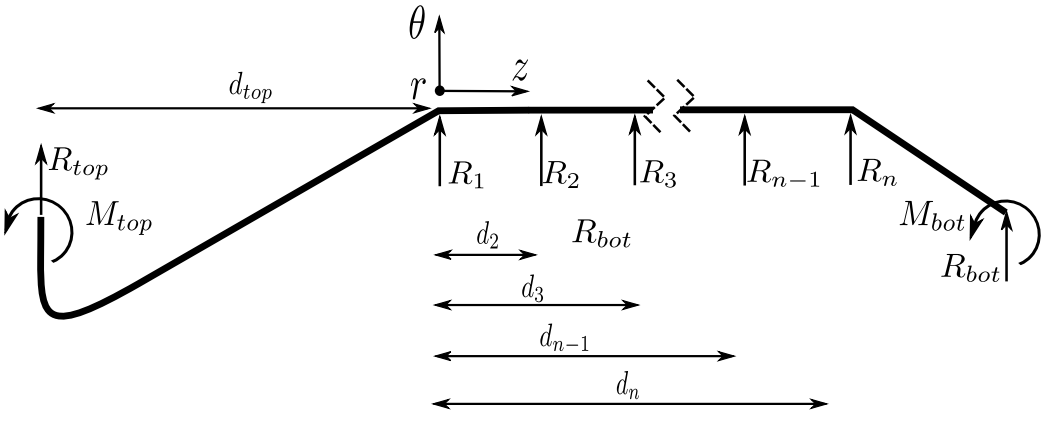

Fig. 9: Reaction forces and moments for the calculation of the bending moment $M(z)$ from $z = 0$ m.

It is important to note that Eq. 24 calculates the longitudinal stress for

a one-dimensional beam element. Therefore, Poisson terms, belonging to the radial σ_r and circumferential σ_θ stress components, are missing, compared with the expression from Goodier (1957) in a generalized plane strain case, for the longitudinal stress σ_z in a cylinder:

$$\sigma_z(r,\theta,z) = \nu(\sigma_r + \sigma_\theta) + \alpha E(\overline{T}_i - T_i) \tag{26}$$

Stress σ_r and σ_θ terms can be added to σ_z expression of Eq. 24, since their value is uncoupled from the longitudinal stress and only depends on the temperature distribution (Montoya et al., 2018). Logie et al. (2018) methodology for plane-strain thermal stress can be used, therefore, σ_r and σ_θ expressions are:

$$\sigma_r = K\frac{\alpha E}{2(1-\nu)}\left[-\ln\frac{b}{r} - \frac{a^2}{b^2-a^2}\left(1-\frac{b^2}{r^2}\right)\ln\frac{b}{a}\right] + K_\theta\frac{\alpha E}{2(1-\nu)}\left(1-\frac{a^2}{r^2}\right)\left(1-\frac{b^2}{r^2}\right) \tag{27}$$

$$\sigma_\Theta = K\frac{\alpha E}{2(1-\nu)}\left[1-\ln\frac{b}{r} - \frac{a^2}{b^2-a^2}\left(1+\frac{b^2}{r^2}\right)\ln\frac{b}{a}\right] + K_\theta\frac{\alpha E}{2(1-\nu)}\left(3-\frac{a^2+b^2}{r^2}-\frac{a^2b^2}{r^4}\right) \tag{28}$$

and introducing Eq. 27 and Eq. 28 in Eq. 26 gives:

$$\begin{aligned}\sigma_z(r,\theta) = {} & K\frac{\alpha E}{2(1-\nu)}\left[1 - 2\ln\frac{b}{r} - \frac{2a^2}{b^2-a^2}\ln\frac{b}{a}\right] \\ & + K_\theta\frac{\alpha E\nu}{1-\nu}\left(2 - \frac{a^2+b^2}{r^2}\right) - \alpha E T_\theta\end{aligned} \tag{29}$$

where the circumferentially varying temperature expression for each segment

340 T_θ is defined using the average geometrical surface temperatures:

$$T_\theta = T - (\overline{T}_{in} - \overline{T}_{out})\frac{\ln \frac{b}{r}}{\ln \frac{b}{a}} - \overline{T}_{out} \tag{30}$$

341 The contribution from the average temperature difference of K and the
342 contribution of circumferential temperature variation on radial and circum-
343 ferential stress K_θ terms on each tube element can be calculated as:

$$K_e = \frac{\overline{T}_{in,e} - \overline{T}_{out,e}}{\ln \frac{b}{a}} \tag{31}$$

344

$$K_{\theta,e} = \frac{rab}{b^2 - a^2}\left[\left(\frac{B_1^{'}b - B_1^{''}a}{a^2 + b^2}\right)\cos\theta + \left(\frac{D_1^{'}b - D_1^{''}a}{a^2 + b^2}\right)\sin\theta\right] \tag{32}$$

345 where $B^{'}, B^{''}, D^{'}, D^{''}$ are Fourier coefficients. Since the formulation assu-
346 mes the temperature field approximated to a plane harmonic Fourier series,
347 it is necessary to approximate the inner and outer temperature distributions
348 to Fourier series as follows:

$$T_{in,e} = \overline{T}_{in,e} + \sum_{v=1}^{\infty} B_{v,e}^{'}\cos v\theta + D_{v,e}^{'}\sin v\theta \tag{33}$$

$$T_{out,e} = \overline{T}_{out,e} + \sum_{v=1}^{\infty} B_{v,e}^{''}\cos v\theta + D_{v,e}^{''}\sin v\theta \tag{34}$$

349 Therefore, introducing terms of coefficients K and K_θ on Eq. 24 leads
350 to the following expression to calculate the thermal stress in a multiple-

supported tube with elbows:

$$\sigma_z(r,\theta,z) = \frac{F_{Te}}{A} + \frac{M(z)}{I} r cos\theta - \alpha E \Delta T + K_e \frac{\alpha E}{2(1-\nu)} \left[1 - 2\ln\frac{b}{r} - \frac{2a^2}{b^2-a^2}\ln\frac{b}{a} \right] + K_{\theta,e} \frac{\alpha E \nu}{1-\nu} \left(2 - \frac{a^2+b^2}{r^2} \right) \tag{35}$$

where F_T and ΔT terms are the contributions of the temperature variation to the stress and are equivalent to the T_θ term from Eq. 29 and $M(z)$ term is the contribution of the bending moments, taken into account the tube mechanical restrictions.

4. Results and discussion

4.1. Verification

The proposed methodology for calculating thermal stress and displacements in receiver tubes has been implemented in Matlab, and verified with already existing models: Logie et al. (2018) methodology for calculating thermal stress, and Khanna et al. (2014) for stress and tube deflection. Khanna et al. (2014) model calculates stress and deflection for straight tube geometries, therefore, two tube geometries has been studied in order to verify the present model: A 18 m straight tube, which corresponds to the straight lenght from Fig. 2, and the complete geometry with elbows, assuming a flat aiming strategy (Fig. 5b) Results have been also compared with the FEM from Montoya et al. (2018), developed using the commercial software Abaqus/Standard. The maximum stress values are located on the tube re-

gion facing the heliostats, therefore, presented results are for $\theta = 0°$ stress on the tube cross-section.

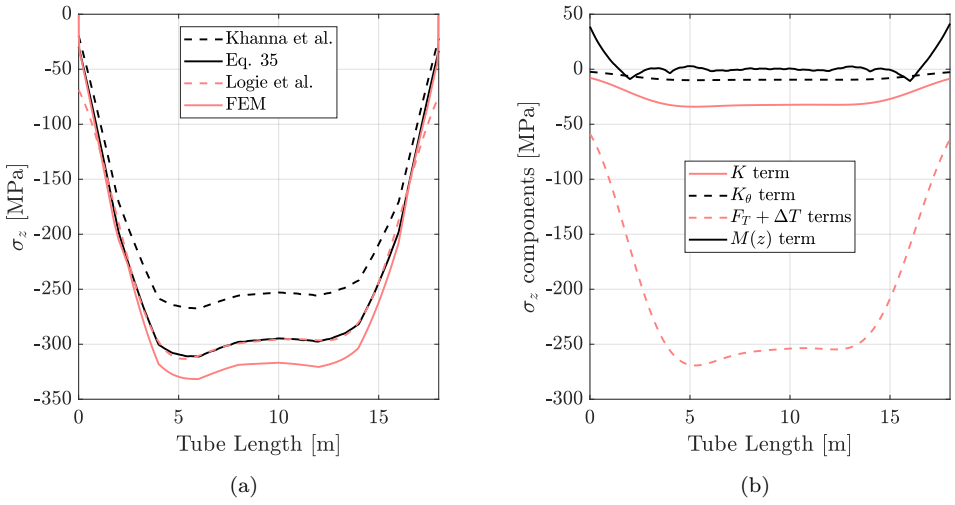

Fig. 10: For the flat aiming strategy and $s = 2$ m a) longitudinal stress comparison in a straight tube, b) components of the longitudinal stress (Eq. 35).

Fig. 10a shows the longitudinal stress σ_z for the straight tube, calculated with the mentioned methodologies for a uniform clips distance s of 2 m. σ_z from Khanna et al. (2014) presents the highest difference compared with FEM, due to the lack of σ_r and σ_θ contribution to the longitudinal stress. The distance between clips is small enough to be considered a plane strain case, the contribution of the bending moment $M(z)$ to the longitudinal stress could be neglected (Fig. 10b). Therefore, σ_z from plane strain problem Logie et al. (2018) results and Eq. 35 are almost the same. The difference between FEM and Eq. 35 is lower than 10%. Note that the terms that mainly affect the thermal stress are those related to temperature variations in the cross-section, F_T and ΔT terms.

The effect of bending moment on longitudinal stress is more noticeable

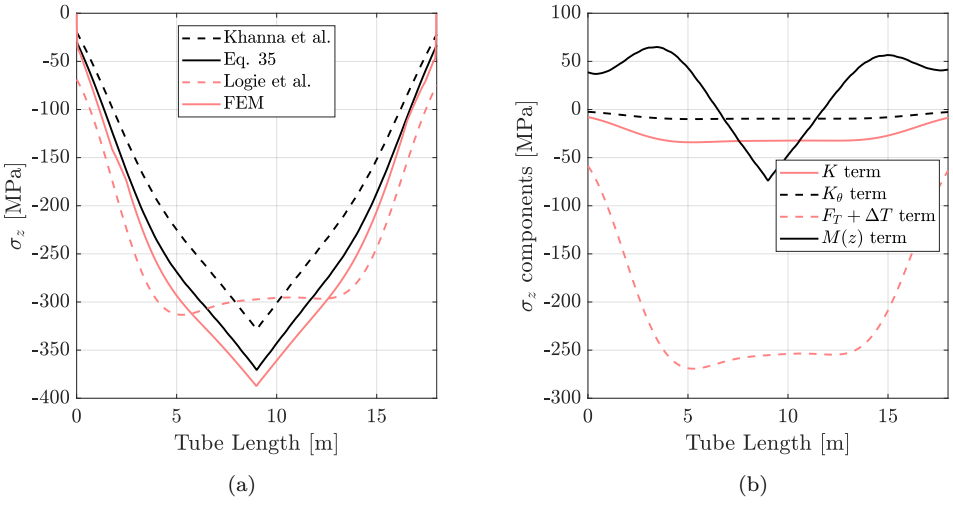

Fig. 11: For the flat aiming strategy and $s = 9$ m a) longitudinal stress comparison in a straight tube, b) components of the longitudinal stress (Eq. 35).

when clips distance s is increased to 9 m (Fig. 11). Fig. 11a depicts how plane strain equation Logie et al. (2018) is unable to capture the longitudinal stress variation correctly. A greater clips separation increases the bending moments along the tube. Fig. 11b shows that $M(z)$ has a higher impact on longitudinal stress, changing the stress distribution along the tube, while the other terms remain constant. As in the previous case, the lack of σ_r and σ_θ contributions underestimate the longitudinal stress value.

The tube deflection u_y (perpendicular to the longitudinal direction) for a straight tube of 18 m compared with the tube with elbows is shown in Fig. 12. The proposed methodology and Khanna et al. (2014) provide for the straight tube, virtually the same displacement. Nevertheless, there is and important difference between results from the straight tube and the real geometry. The elbows stiffen the tube, so the deflection is lower at the straight length ends. On the central region of the tube, the influence of the boundary conditions

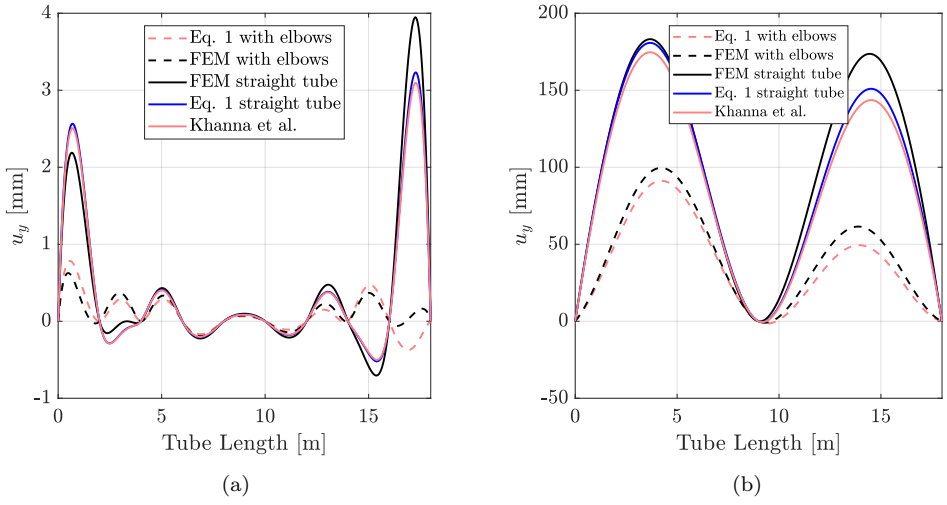

Fig. 12: Displacement comparison for the flat aiming strategy of the tube with elbows and straight tube for a) $s = 2$ m b) $s = 9$ m. Only the deflection along the straight length is depicted.

from the ends decreases, therefore, displacement is almost the same for z between 6 and 12 m in Fig. 12a. When there are lesser clips (Fig.12b) the influence of boundary conditions at tube ends affects the entire tube length, and the displacement differs in the central tube part also. The effect of tube elbows is considered with the direct stiffness methodology, and displacement results are similar to FEM, something that can not be achieved without considering the complete tube geometry.

Moreover, there is a sightly difference between results from FEM and the analytical solution, especially at tube ends. FEM is a 3-D model that takes into account the thermal expansion of the tube cross-section, it can not be done using a 1-D analytical model. Mechanical boundary conditions also differ, since in FEM they are placed in the rear tube face ($\theta = 180°$). In the proposed analytical model, boundary conditions are placed at nodes, without

considering their position in the tube section. Despite these differences, the relative error between the maximum displacement of FEM and the proposed model, for an straight tube (Fig. 12a solid blue and black lines), is around 22%, being the reference value the FEM. The presented model has a reduced computational cost, being more than 20 times faster than FEM in the same computer.

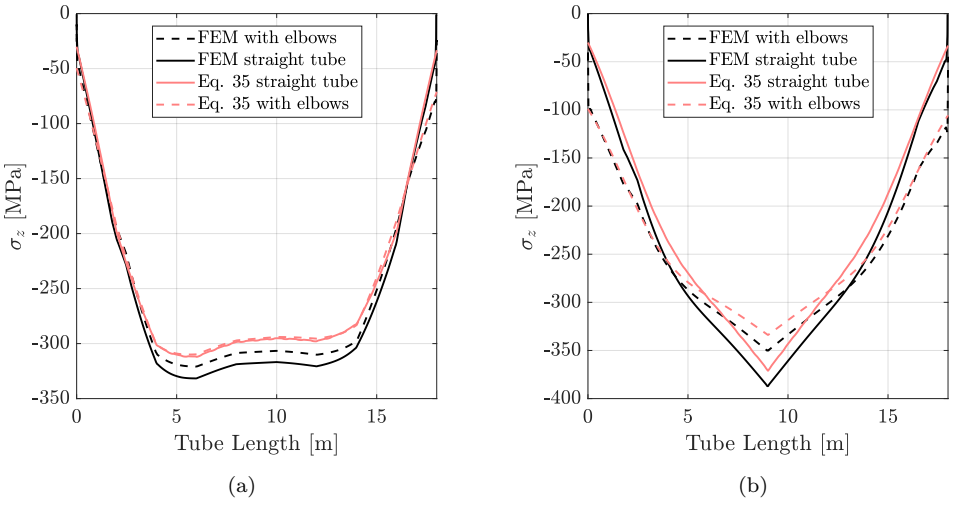

Fig. 13: Stress comparison, for the flat aiming strategy, of the tube with elbows (along the straight length) and the straight tube for a) $s = 2$ m b)$s = 9$ m.

Fig. 13 presents similar thermal stress between the straight tube and the tube with elbows. The boundary conditions at the tube ends also influence the longitudinal stress, but to a lesser extent compared with displacement. The difference between the real tube stress and a straight tube under the same temperature field is around 3% (Clips distance of 2 m, Fig. 13a) and 10% (Clips distance of 9 m, Fig. 13b). As the case is close to the plane strain problem, the influence of the boundary conditions at tube ends is lower. Therefore, considering a straight tube is a good approximation of the

stresses for tube geometries with elbows, when clip distance is equal or lower than 2 m.

4.2. Influence of distance between clips

To observe the effect of the mechanical boundary conditions in the thermal stress in receiver tubes, the influence of clip distance in deflection and thermal stress, in a tube with elbows, has been studied. The two temperatures distribution from Fig. 5 has been considered for the geometry of Fig. 2, to compare the results obtained from the two aiming strategies studied: a flat aiming strategy, and a equatorial one.

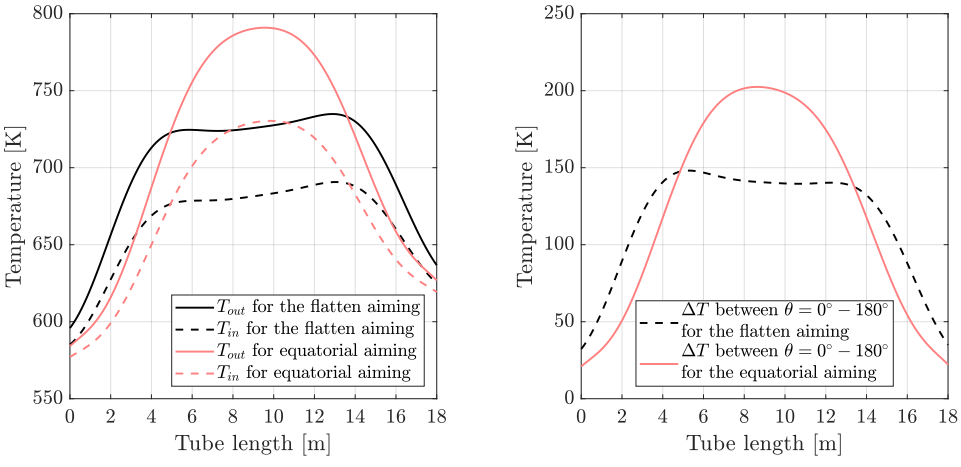

Fig. 14: Along the straight tube length of a tube with elbows, a) Temperature longitudinal variation on the front face ($\theta = 0°$) b) temperature difference between $\theta = 0°$ and $\theta = 180°$ for flat and equatorial aiming strategies.

For a better understanding of the longitudinal temperature variation for each aiming strategy along the straight tube part, the temperature on the tube area facing the heliostats ($\theta = 0°$) is presented in Fig. 14a. The

temperature difference between the front tube face, $\theta = 0°$, and the rear face, $\theta = 180°$ is presented in Fig. 14b. This difference produces the tube bending, due to the different thermal expansion between the hot and cold tube faces (Montoya et al., 2018, 2019).

The following figures present, along the tube straight length, the tube deflection u_y calculated using Eq. 1 and equivalent stress σ_{eq} (the Von Mises stress formula), where shear stress components are negligible (Montoya et al., 2018):

$$\sigma_{eq} = \sqrt{\sigma_r^2 + \sigma_\theta^2 + \sigma_z^2 - (\sigma_r\sigma_\theta + \sigma_\theta\sigma_z + \sigma_r\sigma_z) + 3(\sigma_{r\theta}^2 + \sigma_{\theta z}^2 + \sigma_{rz}^2)} \quad (36)$$

Fig. 15 shows the deflection and the equivalent stress for the flat aiming strategy, while Fig. 16 shows the same variables for the equatorial aiming strategy along the tube straight length. Clip distance s takes values of 1, 1.5, 2, 3, 4.5, 6 and 9 meters, in order to study how stress and displacement change when clips distance increases.

For both aiming strategies, the displacement does not increase significantly for clip distance lower than 2 meters (Figs. 15a and 16a), being the maximum value lower than 1 mm. Clip distance is small enough to do not influence the equivalent stress, being to the plane strain case. When s increases, the tube deflection increases, having the highest value for $s = 9$ m (3 clips along the tube). Clips have also influence on thermal stress. When clips separation lower than $s = 2$ m, σ_{eq} has a similar variation than the temperature along tube length, without changing its maximum value. When the clips distance increases, the tube deformation increases, and the bending

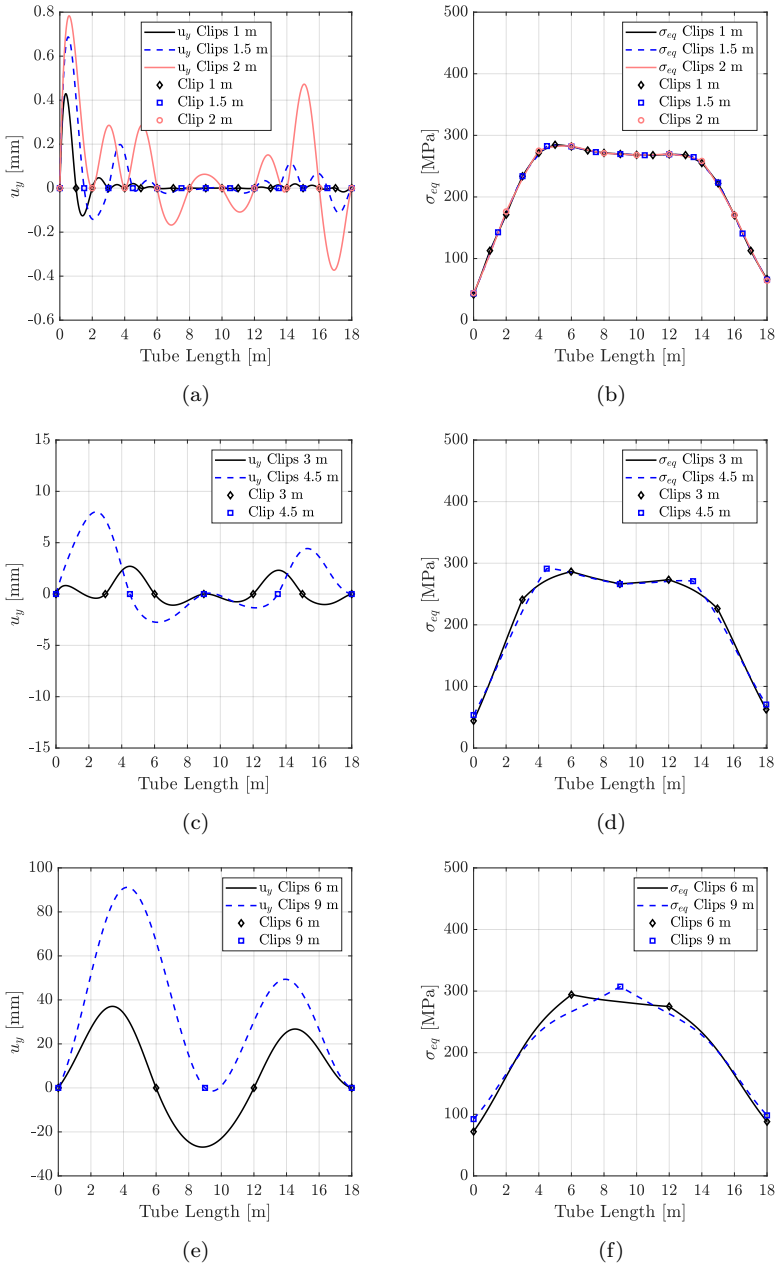

Fig. 15: Along the straight length of a tube with elbows for a flat aiming strategy, tube deflection (left figures) and equivalent stress (right figures)for s from 1 to 9 m. Note de the different y-axis scale in the displacement figures.

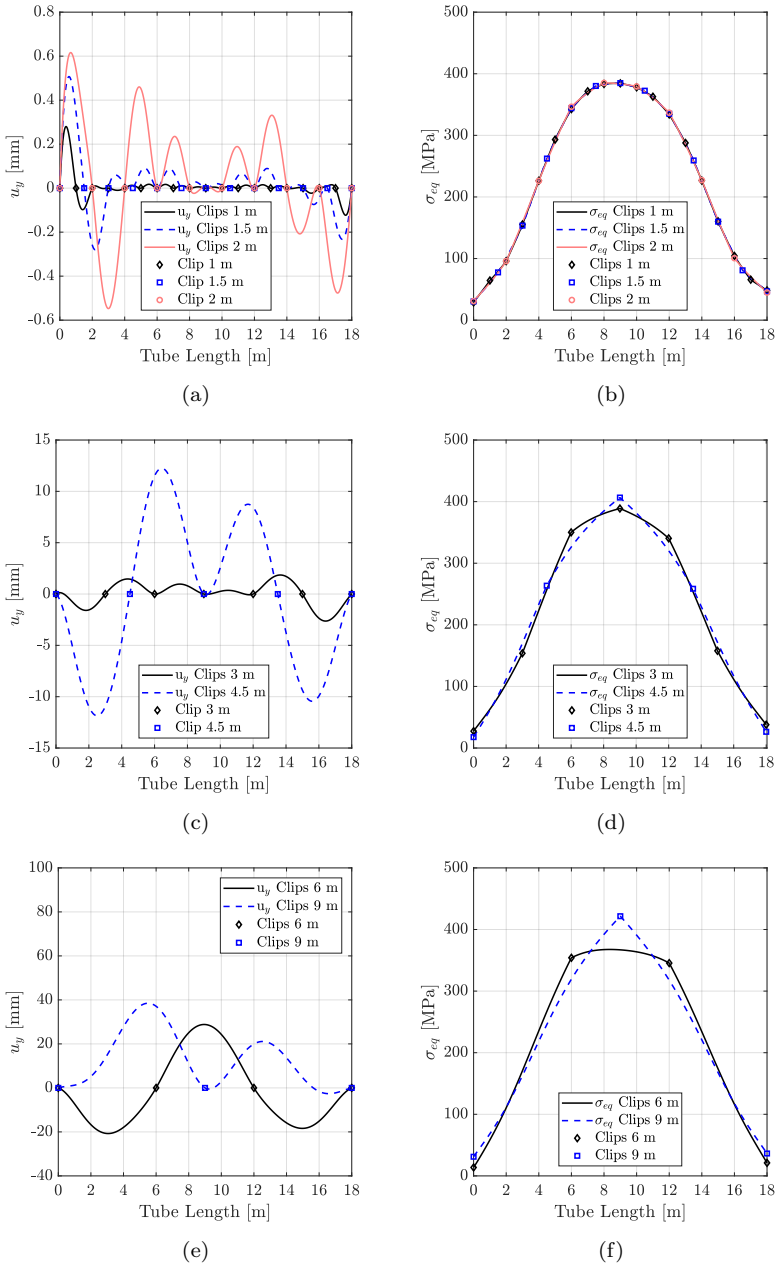

Fig. 16: Along the straight length of a tube with elbows for a equatorial aiming strategyW, tube deflection (left figures) and equivalent stress (right figures)for s from 1 to 9 m. Note de the different y-axis scale in the displacement figures.

moment becomes more important, changing the longitudinal stress along the tube.

Table 3 contains the equivalent stress and displacement values for both aiming strategies and different clip distances. It can be observed how displacement is lower for an equatorial aiming strategy than for a flat one, although the temperature is higher for the equatorial aiming strategy. Tube ends, where the straight tube part is connected to the elbows that fix the tube to the bottom and top headers, have a lower stiffness than the central tube region. Temperature for the flat aiming strategy is higher near the elbows, so the displacement is higher on the tube ends, especially for $z = 0$ m, where the HTF enters, due to the lower stiffness of the top elbow compared with the bottom one.

Table 3: Maximum equivalent stress and displacement values from Fig. 15 and Fig. 16

	Flat aiming		**Equatorial aiming**	
s[m]	$\sigma_{\mathbf{eq}}$[MPa]	$\mathbf{u_y}$[mm]	$\sigma_{\mathbf{eq}}$[MPa]	$\mathbf{u_y}$[mm]
1	284.68	0.43	384.43	0.28
1.5	283.74	0.68	384.88	0.51
2	282.80	0.78	385.06	0.62
3	286.38	2.70	388.81	1.85
4.5	291.21	8.00	406.60	12.24
6	294.18	37.05	367.59	28.82
9	307.25	91.17	421.60	38.42

Thermal stress is greater for the equatorial aiming strategy, since the temperature difference between the front and rear tube faces (Fig. 14b) is also higher. There is no significant change in the maximum stress value with lower s than 2 m. It increases for $s = 3$ m and above, but the difference between σ_{eq} for all the clip distances is lower than 10%. Note that, for $s = 6$

m and a equatorial aiming, the equivalent stress is lower compared with others values of s. Not having clips at the central part of the tube allows the stress to decrease, because the peak temperature is located at the central tube region. For $s = 9$ m, a clip is located in the middle of the tube length, so the stress increases drastically.

5. Conclusions

In this study, an analysis of the deflection and stresses in tubular central receivers has been carried out. An analytical methodology to obtain the tube deflection and stresses in a receiver with elbows has been presented and compared with existing methodologies and a finite element model. The influence of longitudinal supports distance on stress and displacement under different aiming strategies has been also studied.

Supports along the tube length, also called clips, are a key factor for the stress and displacement in tubular central receivers. The tube deflection has been calculated with the proposed methodology, using the direct stiffness method. When results are compared with a finite element model, the analytical methodology only differs sightly at the tube ends, due to the difference in boundary conditions between the 1-D model and the 3-D FEM model. The methodology developed takes into account the actual tube geometry, with elbows, and the computational cost is around 20 times lower than the finite element analysis.

To obtain an accurate stress distribution, when the number of clips is low, it is necessary to calculate the bending moment along the tube. The bending moment is the sum of the mechanical moments produced by restraints along

the tube and the thermal moments. Contributions from radial and circumferential stress to the longitudinal stress should be added for a more accurate stress calculation. The resultant equation gives the longitudinal stress value for receiver tubes, independently of the number of clips. When the clip distance is small, the curvature of the tube is lesser, so plane strain solution estimates properly the thermal stress.

To study the clips influence on stress and deflection, two aiming strategies have been compared, with heliostats aiming to the receiver equator, or trying to flatten the heat flux along the receiver. For each aiming strategy, different distances between clips have been studied, from 1 m to 9 m. Results show that displacement increases with the distance between clips. With a distance lower or equal to 2 m, the deflection for both aiming strategies is lower than 1 mm. For greater clip distances, the displacement increases considerably. The maximum displacement value is always located at tube ends, because of the lower stiffness of this region, compared with the central part. The deflection is higher for a homogenised temperature distribution (flat aiming strategy), due to the greater temperature at the tube ends, compared with an equatorial aiming strategy, so the displacement is also higher.

The thermal stress distribution along the tube for a small distance between clips is similar to the temperature distribution. When the clip distance is greater than 2 m, the stress distribution starts to change and differs from the temperature, because the slope variation at each clip is more remarkable. The highest stress value, for small clip distances, is located where the difference between the temperature of the front tube face and the rear face is. When the distance increases, maximum stress is located where there is a clip.

The highest stress does not increase significantly until the distance between clips is 3 m or more. Therefore, to reduce the displacement and have a stress distribution close to the plane strain problem under the studied conditions, a clips distance of 2 m it is recommended.

Nomenclature

Roman symbols

A	tube cross section area [m^2]
a	tube inner radius [mm]
B, D	Fourier coefficients
b	tube outer radius [m]
C_1, C_2	constants of integration
d	clips distance from the coordinate system origin [m]
E	Young's modulus [Pa]
$\vec{\mathbf{F}}$	nodal forces vector
F	Force [N]
$\vec{\mathbf{f}}$	element forces vector
$\hat{\vec{\mathbf{f}}}$	element forces vector in local coordinates
f	nodal element forces [N]
I	area moment of inertia [m^4]
J	number of elements
$\mathbf{K}$	global stiffness matrix
K	geometric thermal stress term [K]
ΔL	element length [m]
L	tube length [m]

M	bending moment [N-m]
m	nodal element bending moment [N-m]
N	number of nodes [N-m]
$\hat{\vec{\mathbf{p}}}$	external forces on nodes in local coordinates
$\hat{\vec{\mathbf{r}}}$	distributed external transformed to nodal forces in local coordinates
r	polar radial coordinate [m]
s	clips separation [m]
$\vec{\mathbf{R}}$	nodal reaction forces vector [m]
R	reaction force [m]
$\mathbf{T}$	transition matrix
T	temperature [K]
$\overline{T}$	mean temperature [K]
ΔT	temperature difference from ambient conditions [K]
$\vec{\mathbf{U}}$	nodal displacements vector
$\vec{\mathbf{u}}$	element displacements vector
$\hat{\vec{\mathbf{u}}}$	element displacements vector in local coordinates
u_y	displacement in perpendicular direction to the tube end [mm]
x	global coordinate [m]
$\hat{x}$	local coordinate [m]
y	global coordinate [m]
$\hat{y}$	local coordinate [m]
z	coordinate in the axial direction [m]

Greek symbols

α	linear thermal expansion coefficient [K^{-1}]

Δ	difference operator
ν	Poisson's ratio
θ	cylindrical angular coordinate [rad]
ρ	tube curvature radius [m]
σ	stress [MPa]
ϕ	rotation angle of an element [rad]

Abbreviations

HTF	heat transfer fluid
FEM	finite element analysis
CFD	computational fluids dynamics

Subscripts

1	first element node
2	second element node
bot	bottom tube weld
in	inner tube surface
e	eth beam element
elbow	tube elbows regions
enc	encastred problem
eq	equivalent stress
HTF	Heat transfer fluid
j	jth clip
out	outer tube surface
matrix	matrix problem

θ	circumferential component
P	rigidly fixed beam problem
R	reduced equations system
r	radial component
st	tube straight length region
top	top tube weld
T	thermal, caused by the temperature
x	x component
$\hat{x}$	x component in the element local coordinate system
y	y component
$\hat{y}$	y component in the element local coordinate system
z	longitudinal component

Acknowledgements

This work has been supported by the Ministerio de Ciencia, Innovacion y Universidades (Projects RTI2018-096664-B-C21 and RTI2018-096664-B-C22 (MICINN/FEDER, UE)) of the Spanish Government and the Iberdrola Foundation Spain under the fellowship "Ayudas a la investigación en energía y medio ambiente 2018".

References

Akbarimoosavi, S. M., Yaghoubi, M., 2013. 3D thermal-structural analysis of an absorber tube of a parabolic trough collector and the effect of tube deflection on optical efficiency. Energy Procedia 49, 2433–2443.

American Society of Mechanical Engineers, 2010. ASME Boiler and Pressure Vessel Code II, part D: Properties (Metric) Materials. Tech. rep., ASME, New York, USA.

Barron, R. F., Barron, B. R., 2011. Design for Thermal Stresses. Engineering case studies online. Wiley, New Jersey.

Du, B. C., He, Y. L., Zheng, Z. J., Cheng, Z. D., 2016. Analysis of thermal stress and fatigue fracture for the solar tower molten salt receiver. Applied Thermal Engineering 99, 741–750.

Gatewood, B. E., 1941. Thermal stresses in long cylindrical bodies. The London, Edinburgh, and Dublin Philosophical Magazine and Journal of Science 32 (213), 282–301.

Gere, J. M., Goodno, B. J., 2012. Mechanics of Materials, 8th Edition. Cengage Learning.

Goodier, J. N., 1937. Thermal stress in long cylindrical shells due to temperature variation round the circumference and through the wall. Canadian Journal of Research 15a (4), 49–58.

Goodier, J. N., 1957. Thermal stresses and deformation. Journal of Applied Mechanics 24 (3), 467–474.

Ho, C. K., 2017. Advances in central receivers for concentrating solar applications. Solar Energy 152, 38–56.

Irfan, M. A., Chapman, W., 2009. Thermal stresses in radiant tubes due to

axial, circumferential and radial temperature distributions. Applied Thermal Engineering 29 (10), 1913–1920.

Jones, J., 1979. Absence of bending effects on solar-receiver-tube fatigue. Journal of Energy 3, 187–190.

Kassimali, A., 2011. Matrix Analysis of Structures, 2nd Edition. CL-Engineering.

Khanna, S., Kedare, S. B., Singh, S., 2013. Analytical expression for circumferential and axial distribution of absorbed flux on a bent absorber tube of solar parabolic trough concentrator. Solar Energy 92, 26–40.

Khanna, S., Kedare, S. B., Singh, S., 2014. Deflection and stresses in absorber tube of solar parabolic trough due to circumferential and axial flux variations on absorber tube supported at multiple points. Solar Energy 99, 134–151.

Khanna, S., Sharma, V., Kedare, S. B., Singh, S., 2016. Experimental investigation of the bending of absorber tube of solar parabolic trough concentrator and comparison with analytical results. Solar Energy 125, 1–11.

Li, L., Sun, J., Li, Y., 2017. Thermal load and bending analysis of heat collection element of direct-steam-generation parabolic-trough solar power plant. Applied Thermal Engineering 127, 1530–1542.

Litwin, R. Z., 2002. Receiver System : Lessons Learned from Solar Two Receiver System : Lessons Learned From Solar Two. Tech. Rep. SAND2002-0084, Sandia National Labs, Canoga Park.

Logie, W. R., Pye, J. D., Coventry, J., 2018. Thermoelastic stress in concentrating solar receiver tubes: A retrospect on stress analysis methodology, and comparison of salt and sodium. Solar Energy 160, 368–379.

Marugán-Cruz, C., Flores, O., Santana, D., García-Villalba, M., 2016. Heat transfer and thermal stresses in a circular tube with a non-uniform heat flux. International Journal of Heat and Mass Transfer 96, 256–266.

McDowell, M., Miner, K., 2013. Concentrating Solar Power Central Receiver Panel Component Fabrication and Testing. Tech. Rep. RD10-158, Pratt & Whitney Rocketdyne, Canoga Park.

Montoya, A., Rodríguez-Sánchez, M. R., López-Puente, J., Santana, D., 2018. Numerical model of solar external receiver tubes: Influence of mechanical boundary conditions and temperature variation in thermoelastic stresses. Solar Energy 174, 912922.

Montoya, A., Rodríguez-Sánchez, M. R., López-Puente, J., Santana, D., 2019. Thermal stress variation in a solar central receiver during daily operation. AIP Conference Proceedings 2126 (1), 030038.

Radosevich, L. G., Skinrood, A. C., 1989. The Power Production Operation of Solar One, the 10 MWe Solar Thermal Central Receiver Pilot Plant. Journal of Solar Energy Engineering 111 (2), 144–151.

Rodriguez-Sanchez, M. R., Sanchez-Gonzalez, A., Marugan-Cruz, C., Santana, D., nov 2014. Saving assessment using the PERS in solar power towers. Energy Conversion and Management 87, 810–819.

Rodríguez-Sánchez, M. R., Soria-Verdugo, A., Almendros-Ibáñez, J. A., Acosta-Iborra, A., Santana, D., 2014. Thermal design guidelines of solar power towers. Applied Thermal Engineering 63 (1), 428–438.

Sánchez-González, A., Rodríguez-Sánchez, M. R., Santana, D., 2017. Aiming strategy model based on allowable flux densities for molten salt central receivers. Solar Energy 157, 1130–1144.

Sánchez-González, A., Rodríguez-Sánchez, M. R., Santana, D., 2018. Aiming factor to flatten the flux distribution on cylindrical receivers. Energy 153, 113–125.

Sánchez-González, A., Santana, D., 2015. Solar flux distribution on central receivers: a projection method from analytic function. Renewable Energy 74, 576–587.

Timoshenko, S., Goodier, J. N., 1951. Theory of Elasticity, 2nd Edition. Vol. 49. McGraw-Hill Book Company.

Uhlig, R., Frantz, C., Flesch, R., Fritsch, A., 2018. Stress analysis of external molten salt receiver. AIP Conference Proceedings 2033 (1), 040040.

Wang, F., Shuai, Y., Yuan, Y., Liu, B., 2012. Effects of material selection on the thermal stresses of tube receiver under concentrated solar irradiation. Materials & Design 33 (Supplement C), 284–291.

Wang, Y., Liu, Q., Jing, L., Jin, H., Lei, J., Jin, H., 2015. Performance analysis of a parabolic trough solar collector with non-uniform solar flux conditions. International Journal of Heat and Mass Transfer 82, 236–249.

Zavoico, A. B., 2001. Solar Power Tower: Design Basis Document. Tech. rep., Sandia National Laboratory, San Francisco, SAND2001-2100.